Journal of
Applied Crystallography
ISSN 1600-5767

addenda and errata

Towards a detailed resolution smearing kernel for time-of-flight neutron reflectometers. Corrigendum

Andrew Robert John Nelson[a,b]* and Charles David Dewhurst[c]

[a]Bragg Institute, Australian Nuclear Science and Technology Organisation, Locked Bag 2001, Kirrawee DC, NSW 2232, Australia, [b]NIST Centre for Neutron Research, National Institute of Standards and Technology, Gaithersburg, MD 20899, USA, and [c]Institut Laue–Langevin, 6 rue Jules Horowitz, BP 156 F-38042, Grenoble Cedex 9, France. Correspondence e-mail: andrew.nelson@ansto.gov.au

In the paper by Nelson [*J. Appl. Cryst.* (2013), **46**, 1338–1346], Charles Dewhurst is missing from the list of authors. The complete list of authors should be A. R. J. Nelson and C. D. Dewhurst.

References

Nelson, A. R. J. (2013). *J. Appl. Cryst.* **46**, 1338–1346.

  doi:10.1107/S1600576714009595

Journal of
Applied Crystallography

ISSN 0021-8898

Received 2 April 2013
Accepted 6 August 2013

Towards a detailed resolution smearing kernel for time-of-flight neutron reflectometers

Andrew Robert John Nelson

Bragg Institute, Australian Nuclear Science and Technology Organisation, Locked Bag 2001, Kirrawee DC, NSW 2232, Australia, and NIST Centre for Neutron Research, National Institute of Standards and Technology, Gaithersburg, MD 20899, USA. Correspondence e-mail: andrew.nelson@ansto.gov.au

In this article a 'detailed' form of the resolution kernel used to analyse data from reactor-based time-of-flight (TOF) neutron reflectometers is derived. In contrast to monochromatic neutron reflectometers, where the resolution kernel is close to Gaussian, TOF neutron reflectometers can have trapezoidal resolution kernels. This is a consequence of the disc chopper systems used to pulse the beam having a wavelength uncertainty that is rectangular in shape. The effect of using the detailed and approximate kernels is compared, with the main effects occurring where the width of the kernel is approximately the same as the width of the features in the reflectivity curve, *i.e.* around the critical edge and at high Q_z. The difference between the two kernels is greatest when the wavelength and angular components are of different sizes.

1. Introduction

Neutron (NR) and X-ray reflectometry (XRR) techniques are widely used for the characterization of interfacial thin films, such as those found in organic light emitting diode displays, biomembranes *etc.* Both methods measure the specularly reflected intensity as a function of momentum transfer, Q_z, from a collimated beam of radiation directed at an interface:

$$Q_{z,0} = (4\pi/\lambda_0)\sin\theta_0, \quad (1)$$

where λ is the wavelength of the radiation and θ is the angle of incidence onto the sample. The subscript 0 denotes that these are the nominal values. The subscript z denotes that only the surface normal component of momentum transfer is considered, *i.e.* the specular reflection. The NR and XRR techniques are complementary, with the key difference being that the X-ray scattering length of a material is proportional to its atomic number (X-rays are scattered by electrons), whereas the neutron scattering length of a material is atom and isotope dependent (neutrons are scattered by the nucleus). This property of neutron scattering allows one to selectively change the scattering contrast within a system, highlighting different components within an interface. Unfortunately, NR suffers the drawback that the source (whether a reactor or spallation source) brilliance is many orders of magnitude lower than most X-ray sources, even the lowly Cu $K\alpha$ tube in a laboratory.

Most neutron reflectometers can be divided into two classes, those that are angular dispersive (Dura *et al.*, 2006) and those that are energy dispersive (Campbell *et al.*, 2011; Webster *et al.*, 2006; James *et al.*, 2011; de Haan *et al.*, 1995). The former use a monochromator to select a specific wavelength band to direct onto the sample – NR measurements are performed at many different angles of incidence. The latter use neutrons with a broad range of wavelengths – NR measurements are taken at two or three different angles of incidence. The energy dispersive instruments make use of time of flight (TOF) to determine the wavelength of each neutron that hits the detector. Energy dispersive measurements have the advantage of being able to measure across a broad range of momentum transfer at a single setting, making them attractive for those who want to carry out kinetic measurements. Energy dispersive reflectometers are found at spallation sources (Webster *et al.*, 2006), and at reactors (Campbell *et al.*, 2011; James *et al.*, 2011; de Haan *et al.*, 1995; Cousin *et al.*, 2011), where the time-of-flight setup is based on the use of choppers to pulse the beam.

To make most efficient use of the available flux, NR measurements are typically performed at a more relaxed Q_z resolution than XRR measurements. There are two main components that contribute to resolution: (1) the angular divergence of the collimated beam, and (2) the wavelength resolution of the radiation (de Haan *et al.*, 1995; van Well & Fredrikze, 2005). It is essential that these resolution terms be accounted for when analysing reflectivity data, because they smear sharp features present in the curves. A typical reflectometry analysis proceeds by creation of a model scattering length density (SLD) profile perpendicular to the interface. The model reflectivity from this profile is easily calculated and can be used in a least-squares analysis – one alters model parameters until the least-squares difference between the model reflectivity and the experimental data is minimized (Nelson, 2006). However, as is the case in most scattering methods, the model reflectivity, R_m, must be convolved with the instrumental resolution kernel, $p(Q_z)$, before comparing with the measured data:

$$R_{m,s}(Q_z) = R_m(Q_z) \otimes p(Q_z). \quad (2)$$

I use the symbol $p(Q_z)$ here to represent the fact that the resolution kernel is a probability density function (PDF).

The functional forms of both the angular and wavelength components are understood and have been explained in detail in articles by de Haan *et al.* (1995) and van Well & Fredrikze (2005). However, van Well and Fredrikze assume that the overall resolution kernel is Gaussian in shape, with the width of this Gaussian being formed by adding the fractional variances of all the components [equation (3)], where there is no correlation between wavelength and angle of incidence:

$$\left(\mathrm{d}Q_z/Q_z\right)^2 = (\mathrm{d}\lambda/\lambda)^2 + (\mathrm{d}\theta/\theta)^2. \quad (3)$$

The justification for this approximation is the central limit theorem. This theorem states that the mean of a large number of independent random variables is approximately normally distributed. Assuming a Gaussian form for the resolution kernel allows one to do the resolution smearing in a straightforward manner and it is also quick. Smearing is typically performed using Gaussian quadrature integration, with 21 points being sufficient for the majority of systems. A similar approach can be used when applying the detailed kernel. In this work a 101 point integration was used for the detailed kernel. Although this slows calculation speed by a factor of five, it limits the size of the error term in the numerical integration. It would have been possible to use a lower number of points, but this varies across measurements, depending on how oscillatory detail is present in $R_m(Q_z)$. The optimum approach in numerical integrations of this kind is to perform an initial adaptive calculation to determine the correct number of integration points for a given system. In any case, a slowdown of a factor of five is insignificant when analyses only take a couple of seconds.

In this article I will calculate the 'detailed' form of the resolution kernel for TOF neutron reflectometers found at reactor sources and compare it with the output from smearing using the Gaussian approximation. Some approximations are still made (such as ignoring gravity), as instrument design in this class of spectrometers is varied.

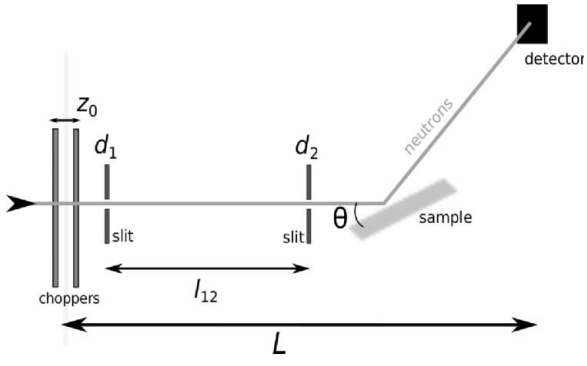

Figure 1
General layout of a TOF neutron reflectometer. In reality the flight length, L, must take into account the longer path followed by a reflected neutron.

2. Detailed kernel computation

2.1. Angular component

The general instrument layout considered in this article is shown in Fig. 1.

For a two-slit collimation system (in the small-angle limit) the angular PDF, $p(\theta)$, is formed by the convolution of two boxcar distributions (Fig. 2*a*).

In Fig. 2(*a*), α and β are given by (de Haan *et al.*, 1995)

$$\alpha = (d_1 + d_2)/(2l_{12}), \quad \beta = |d_1 - d_2|/(2l_{12}), \quad (4)$$

where d_1 and d_2 are the collimation slit heights and l_{12} is the distance between the slits. This takes the form of a trapezoid unless d_1 equals d_2; then the function is triangular. However, we need to have the PDF as a function of Q_z, $p_\theta(Q_z)$, so must use a Jacobian transform to make Q_z the variable of interest:

$$p_\theta(Q_z) = p(\theta)\left|\frac{\partial\theta}{\partial Q_z}\right| = \frac{\lambda_0}{4\pi\cos\theta}p(\theta). \quad (5)$$

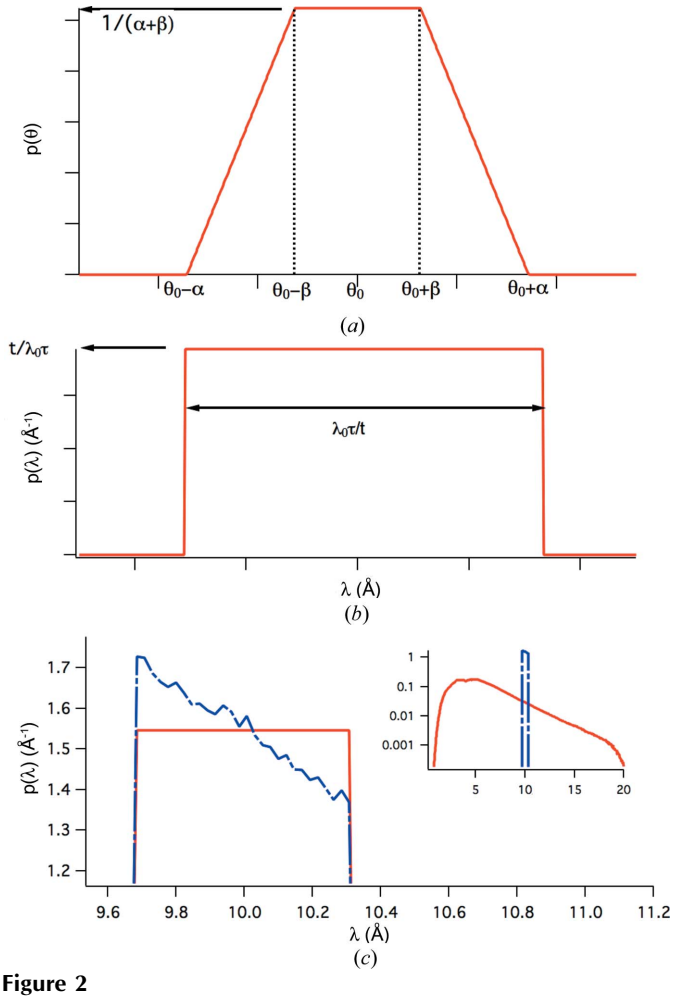

Figure 2
(*a*) The normalized PDF for the angular distribution of the angle of incidence. (*b*) The normalized PDF for the wavelength uncertainty (the FWHM of a Gaussian approximating a boxcar distribution is 0.68 times its width). (*c*) The solid line represents $p_c(\lambda)$ for λ_0 = 10 Å, with τ_c/t = 0.0644. The dashed line represents $p_c(\lambda)$ corrected for the source wavelength spectrum. The graph inset shows a representative Platypus (James *et al.*, 2011) wavelength spectrum and $p_c(\lambda)$.

To calculate $p_\theta(Q_z)$ for a given angle of incidence, θ_0, one first determines the nominal neutron wavelength required to produce that Q_z value, λ_0. We then calculate the normalized function $p(\theta)$. For each θ in $p(\theta)$, calculate the corresponding Q_z value using the nominal wavelength. $p_\theta(Q_z)$ at that Q_z point is then given by equation (5).

2.2. Wavelength component

The various contributions to the wavelength component are explained in detail by van Well & Fredrikze (2005). There are three main components that we will discuss here, which all have PDFs that are rectangular in shape. Each of these components relates to an uncertainty in the total flight time, which corresponds to an uncertainty in wavelength. The principal component is due to the TOF contribution of the chopper disc system, referred to as the 'burst' time, τ_c (Fig. 3*a*). The burst time is the total time that all neutrons of a given wavelength take to find their way through the chopper disc system.

For a double-disc chopper system the following applies:

$$\tau_c = \xi/\omega + z_0 m_n \lambda/h. \tag{6}$$

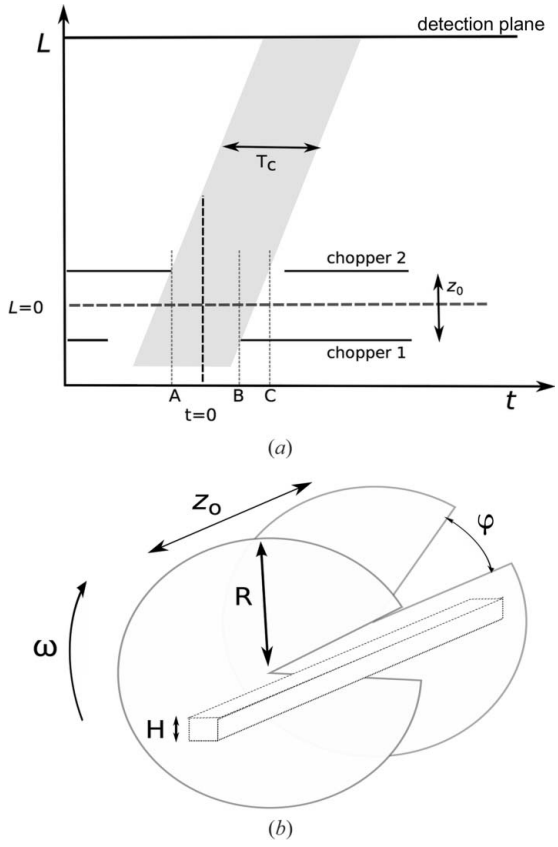

Figure 3
Distance–time diagram for a double-chopper reflectometer. t = A − B corresponds to the first term in equation (6) and t = C − B the second. The situation where the leading edge of chopper 2 coincides with the trailing edge of chopper 1, A = B, corresponds to a zero phase angle. (*b*) A double-disc chopper, each with radius R and rotating with angular velocity ω, crosses a beam of height H.

Here ξ is the phase opening between the two discs (in radians), ω is the angular velocity of the chopper discs (rad s^{-1}), z_0 is the distance between the chopper discs, m_n is the mass of a neutron and h is Planck's constant. A phase opening of zero means that the leading edge of the slave chopper is aligned with the trailing edge of the master chopper. The fractional wavelength resolution is expressed as

$$\tau/t = \Delta\lambda/\lambda, \quad \text{with} \quad t = Lm_n\lambda/h, \tag{7}$$

where t is the total flight time for a given wavelength neutron and L is the length of the neutron flight path. Combining equations (6) and (7) gives

$$\frac{\Delta\lambda}{\lambda} = \frac{\tau_c}{t} = \frac{\xi h}{\omega L m_n \lambda} + \frac{z_0}{L}. \tag{8}$$

Note that if the phase angle is zero then the first part of equation (6) disappears, and the fractional wavelength resolution for this component is equal to z_0/L and is independent of wavelength. Note that the proportionality between τ and λ only applies for wavelengths smaller than $h\varphi/(m_n z_0 \omega)$, where φ is the angular opening of the chopper disc window (radians).

A zero phase angle is the normal operating mode of most double-chopper TOF reflectometers. One of the advantages of a phase opening is that the transmission of the chopper system is greatly increased for shorter-wavelength neutrons, which aids kinetic measurements at higher Q_z values (Mueller-Buschbaum *et al.*, 2007). The origin of the length L is the midpoint between the two chopper discs. The flight time is started from the middle of the rectangular neutron pulse as it passes the midpoint between the two choppers. If the phase angle is zero then t = 0 corresponds to the trailing (leading) edge of disc 1 (2). Otherwise the origin for t is phase angle dependent.

For instruments with a single chopper disc the burst time is given by

$$\tau_c = \varphi/\omega. \tag{9}$$

Thus, for a given chopper setting the fractional wavelength resolution, $\Delta\lambda/\lambda(= \tau_c/t)$, is inversely proportional to wavelength. Resolution improves if the rotation speed is increased, if the total flight time is increased or if the window opening is decreased.

The second major component is due to the width of the time channel histograms in the data acquisition system, $\tau_{DA}(\lambda)$. Narrow time bins are often used during acquisition, which does not affect resolution significantly. However, the use of narrow bins means that the data can appear noisy. Consequently, a 'rebinning' step is often applied during data reduction, which pools bins together: thereby smoothing the data but coarsening the resolution at the same time. The typical bin width is chosen to be proportional to time of flight; as $\tau_{DA}(\lambda)/t$ increases then $\Delta\lambda/\lambda$ for this component increases proportionally.

The third component, which is much smaller in size, is due to the chopper window (which is at radius R from the axle of the chopper) taking a finite time to cross the neutron beam. This is often called the 'crossing' time. If one assumes that the

chopper system is placed just before the collimation slits, then to a first approximation the beam height, H, is equal to the height of the first collimation slit (d_1) and the uncertainty in time of flight is

$$\tau_{\rm h} = H/(\omega R). \quad (10)$$

In such a situation, the PDF for the crossing time component, $p_{\rm h}(\lambda)$, is boxcar in shape (Fig. 2*b*). However, if the collimation system is some distance after the chopper discs, the beam height profile in the chopper system (that would be accepted by the collimation systems) is divergent and would be similar to Fig. 5 of de Haan *et al.* (1995), giving the distribution for $p_{\rm h}(\lambda)$ shown in Fig. 4.

In Fig. 4, $x_1 = [|d_1 - d_2|/(2L_{12})]L_{1c} + d_1/2$ and $x_2 = [(d_1 + d_2)/(2L_{12})]L_{1c} + d_1/2$, L_{1c} is the distance from the first chopper disc to the first collimation slit, and $F = \lambda_0/(\omega R t)$. In the limit where $L_{1c} = 0$, then x_1 and x_2 reduce to $d_1/2$, and Fig. 4 has a boxcar shape. In this article I assume that the crossing time is given by equation (10). The calculations shown here are for crossing times where the collimation system is collinear with the chopper system, with no extra 'bounces' from guides in between the optical components.

If the wavelength spectrum of the source is flat, then the PDFs for the TOF wavelength component [$p(\lambda_{\rm c})$] and the time bin component [$p(\lambda_{\rm DA})$] are boxcar distributions. However, in real life the neutron spectrum supplied to such an instrument is typically Maxwell–Boltzmann in shape. Thus, to obtain the overall PDF for the wavelength component, the PDFs for the individual components must first be convolved with each other, then multiplied by this spectrum (as transmitted by the choppers) and subsequently normalized to unity. The requirement for this multiplication step can be understood more clearly if one considers what would happen to the resolution function if a monochromatic beam were supplied to the instrument. In such a case the wavelength distribution transmitted through the instrument would be narrower than the boxcar distribution and the uncertainty in wavelength would be overestimated. The effect of multiplying by the source spectrum is shown in Fig. 2(*c*). A similar argument should also be applied to the angular component, if the guides supplying the instrument cannot supply the angular divergence accepted by the slits.

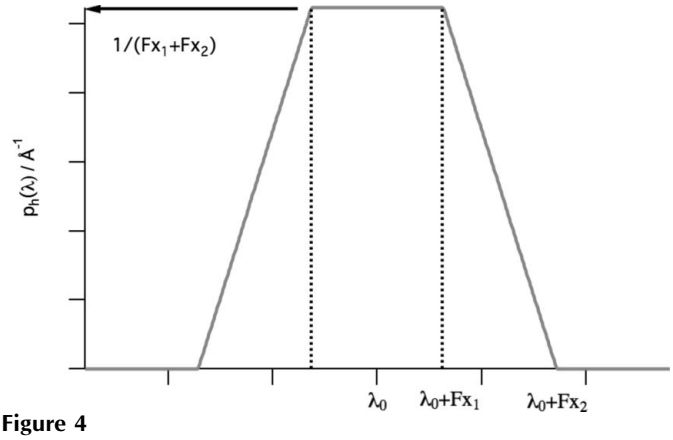

Figure 4
Distribution of wavelengths for the crossing time component, when a divergent beam passes through the chopper system.

These $p(\lambda)$ are transformed to Q_z space with the following relation (Fig. 5):

$$p_\lambda(Q_z) = p(\lambda)\left|\frac{\partial\lambda}{\partial Q_z}\right| = \frac{4\pi\sin\theta_0}{Q_z^2}p(\lambda). \quad (11)$$

2.3. Expected value of $p(Q)$ and comparison with nominal Q value

The expected value of $p(Q_z)$ is given by equation (12). It is not necessarily the case that the expected Q_z value, $\langle Q_z\rangle$, is equal to the nominal $Q_{z,0}$ value calculated from the nominal wavelength and angle of incidence. In the situation where $p(\lambda)$ and $p(\theta)$ are as shown in Figs. 2(*a*) and 2(*b*), then $\langle Q_z\rangle$ for

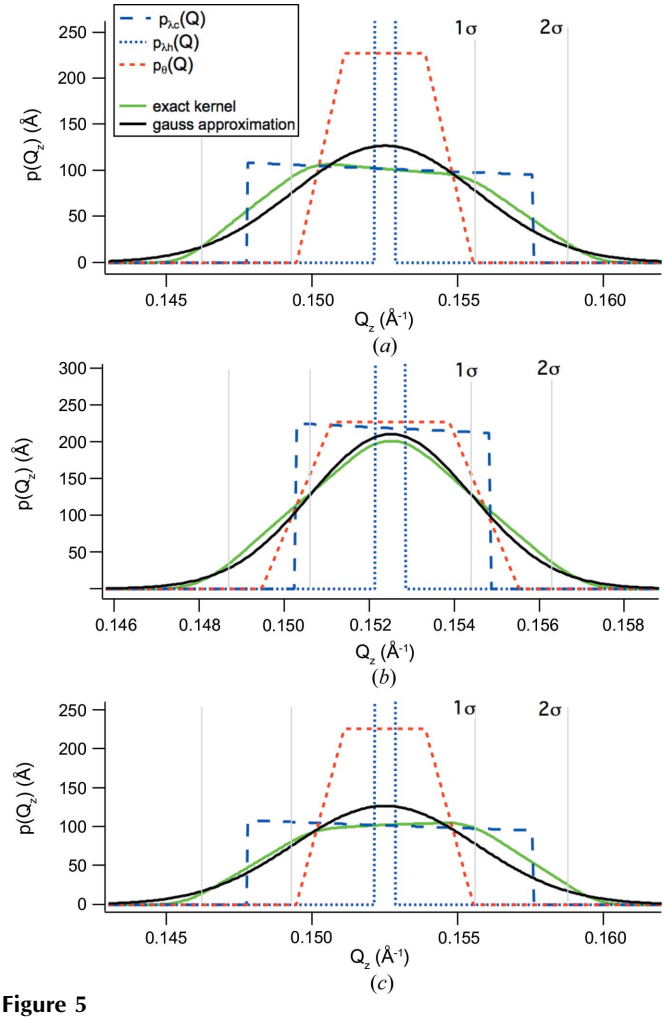

Figure 5
Components contributing to the detailed kernel (solid green line). $p_{\lambda c}(Q_z)$ (dashed blue line) corresponds to the burst time contribution, and $p_{\lambda h}(Q_z)$ (dotted blue line) corresponds to the contribution from the finite height of the beam. Also shown is the Gaussian approximation to the detailed kernel (black line). L_{12} = 2800 mm, d_1 = 4.52 mm, d_2 = 1.69 mm, $\theta_0 = 3.2^\circ$, λ_0 = 4.6 Å. (*a*) $\tau_{\rm c}/t = 0.0644$. (*b*) $\tau_{\rm c}/t = 0.03$. (*c*) Kernel produced by $\theta_0 = 11^\circ$, λ_0 = 15.71 Å, and the same wavelength and angular resolutions as (*a*). The overall kernels are corrected for the source spectrum shown in Fig. 2(*c*).

$p_\lambda(Q_z)$ and $p_\theta(Q_z)$ can be evaluated analytically. When the source spectrum is not constant (Fig. 2*c*), then $\langle Q_z \rangle$ must be integrated numerically from the overall kernel:

$$\langle Q_z \rangle = \int_{-\infty}^{\infty} Q_z \, p(Q_z) \, \mathrm{d}Q_z. \quad (12)$$

2.3.1. Example $\langle Q_z \rangle$ calculation for $p_\lambda(Q_z)$. Assume that $\lambda_0 = 16$ Å, with $\tau_c/t = 0.1$, a flat source spectrum and $\theta_0 = 6^\circ$. We then have $Q_{z,0} = 0.08210$ Å^{-1}. The following applies:

$$p(\lambda) = \begin{cases} t/(\tau_c \lambda) = 0.625 \text{ Å}^{-1}, & 15.2 < \lambda/\text{Å} < 16.8, \\ 0, \end{cases} \quad (13)$$

giving

$$p_\lambda(Q_z) = \begin{cases} 0.625 \, \dfrac{4\pi \sin\theta_0}{Q_z^2} \text{ Å}, & 0.07819 < Q_z/\text{Å}^{-1} < 0.08642, \\ 0, \end{cases} \quad (14)$$

and

$$\langle Q_z \rangle = 0.625(4\pi \sin\theta_0) \int_{0.07819}^{0.08642} 1/Q_z \, \mathrm{d}Q_z = 0.08216 \text{ Å}^{-1}. \quad (15)$$

The difference between $Q_{z,0}$ and $\langle Q_z \rangle$ is minimal: less than 0.1%. The percentage difference between the two is constant as a function of λ_0. However, if $p(\lambda)$ is weighted by the source spectrum shown in Fig. 2(*c*), then $\langle Q_z \rangle$ increases to 0.08232 Å^{-1}, a difference of 0.2%. This is still only a very small difference and would not normally make a huge difference during data analysis. However, this difference increases in size as the wavelength resolution is relaxed further. Here I have only shown a calculation of $\langle Q_z \rangle$ for the burst time component. Similar numerical integrations can be carried out for each $p(Q_z)$ component, including the overall resolution kernel. It is also important to remember that, whilst the difference between $Q_{z,0}$ and $\langle Q_z \rangle$ may not be large, the distribution of $p(Q_z)$ about $\langle Q_z \rangle$ is of consequence, as we shall see later.

2.4. Combined resolution kernel

The combined resolution kernel is obtained by convolving all $p(Q_z)$ components. Figs. 5(*a*) and 5(*b*) show example calculations for a nominal angle of incidence of 3.2° and a nominal wavelength of 4.6 Å, resulting in a nominal Q_z value of 0.1525 Å^{-1}. The various instrument parameters are listed in the caption. For this calculation I have assigned the histogram time channel width term, $p_{\lambda_{DA}}(Q_z)$, to zero. The Gaussian approximation to the smearing kernel [as calculated following van Well & Fredrikze (2005)] is also displayed. From now on I will refer to the fractional Q_z resolution of a measurement as the FWHM of the Gaussian approximation to the detailed kernel divided by the nominal Q_z value. The FWHMs of the Gaussian approximations in Figs. 5(*a*) and 5(*b*) were 0.0074 and 0.0044 Å^{-1}, respectively, corresponding to fractional Q_z resolutions of 4.85 and 2.9%, respectively. Figs. 5(*a*) and 5(*b*) both have the same fractional angular resolution, 2.09%, but they differed in wavelength component: 4.38 and 2.04%.

It is immediately obvious from Fig. 5(*a*) that the detailed resolution kernel is trapezoidal in shape, because the wavelength resolution is broader than the angular component. One also observes that owing to the change of variable $p_\lambda(Q_z)$ is no longer flat for $\lambda_0[1 - \tau_c/(2t)] < \lambda < \lambda_0[1 + \tau_c/(2t)]$, but has a rough slope of Q_z^{-2} [*cf.* equation (11)]. The overall $p(Q_z)$ in Fig. 5 has been corrected for the source spectrum (shown in Fig. 2*c*), but this effect is negligible for Figs. 5(*a*) and 5(*b*) as the spectrum is roughly flat at these wavelengths. In Fig. 5(*b*) the angular and wavelength components are more evenly matched, with the result that the total resolution kernel is now triangular in shape and appears more similar to the Gaussian approximation. However, the overall behaviour of Figs. 5(*a*), 5(*b*) and 5(*c*) is that within 1σ of the nominal Q_z value the detailed resolution kernel is less probable than the Gaussian approximation, but between 1σ and 2σ the situation reverses. This immediately reveals that the Gaussian approximation underestimates the smearing for a TOF neutron reflectometer.

Fig. 5(*c*) shows the resolution kernel for the same Q_z value, using the same wavelength and angular resolution as Fig. 5(*a*) but simulated at higher incident angle and with a longer wavelength. This figure shows the slope at the top of the $p(Q_z)$ profile reversing, a consequence of the $\sim\lambda^{-5}$ tail of the source spectrum. Fig. 5(*c*) also illustrates one other detail, mentioned above. The detailed $p(Q_z)$ is shifted towards higher Q_z compared to the Gaussian approximation. $\langle Q_z \rangle$ for the detailed $p(Q_z)$ is 0.1529 Å^{-1}, but $Q_{z,0}$ is 0.1525 Å^{-1}. More importantly, the $p(Q_z)$ distribution is not symmetric but is skewed towards higher Q_z.

The fact that the detailed resolution kernel is most similar to the Gaussian approximation when both contributions are matched in width (Fig. 5*b*) suggests that it is the optimal measuring condition, providing the overall resolution is suitable for the system being measured. Unfortunately this is often unachievable. For a double-disc chopper system the wavelength resolution is dictated by the distance between the chopper discs compared to the total flight length. If the chopper discs cannot be moved towards, or further away from, each other, then the wavelength resolution is fixed for that chopper pairing (unless phase opening is used). If the default wavelength resolution is 3.5%, the required angular resolution would also be 3.5% (giving an overall resolution of ~5%). However, if the footprint of the sample is short and the sample is to be under-illuminated, then it may only be possible to produce an angular resolution that is much lower, corresponding to the situation in Fig. 5(*a*). Even if the angular resolution is relaxed the sample can become over-illuminated, with the result that the sample acts as a slit, putting an upper limit on the attainable angular resolution. Sometimes another disc pairing is available that gives better wavelength resolution, but these situations are likely to be unacceptable owing to the loss of flux.

For a single-disc chopper TOF reflectometer, or if phase opening ($\xi > 0$) is used on a double-chopper instrument to boost flux, the two components can never be matched. This leads to a transition in the shape of the resolution kernel, with Fig. 5(*a*) applying at low Q_z (resolution is poor for low

wavelengths) and Fig. 5(*b*) applying at high Q_z (resolution is better at higher wavelengths).

It is worth noting at this point that $p(\lambda)$ from a monochromatic reflectometer is typically Gaussian in shape. When this is convolved with the trapezoid of $p(\theta)$, which is similar in width, the detailed resolution kernel will be close to the Gaussian approximation.

Existing TOF reflectometers at spallation sources have quite short burst times because the proton pulse has a short duration. Consequently, their wavelength resolution tends to be excellent compared to the angular component. These instruments typically rebin in wavelength [adjusting the size of $\tau_{DA}(\lambda)$] to give a smoother data set. The optimal rebinning situation would be to match the sizes of the wavelength and angular resolution components. In such a case the overall resolution kernel should be fairly similar to Fig. 5(*b*), with little benefit from computation of the detailed kernel. Only when the rebinning process becomes much coarser than the angular component is kernel computation worthwhile. However, the long pulse length at the European Spallation Source may lead to a broad wavelength resolution at instruments built there unless pulse shaping is employed. These instruments would benefit from computation of the detailed resolution kernel, using the techniques outlined here.

3. Comparison of the smearing effects of the detailed resolution kernel and its Gaussian approximation

The differences between the two smearing kernels will be most evident when the width of the resolution kernel is similar to the width of the features present in the reflectivity curve. For example, thin monolayer films have widely spaced Kiessig fringes. This means that the difference between the detailed and approximate kernels will probably be unnoticeable. For very thick films the Kiessig fringes are closely spaced, with the fringe spacing obeying the relation $\Delta Q_z = 2\pi/d$, d being the layer thickness. The kernel shown in Fig. 5(*a*) has an FWHM of 0.0074 Å^{-1}. If this were the fringe spacing for a single-layer film, then the film thickness would be 850 Å. One expects the differences between the detailed and approximate forms to become more visible at higher Q_z. This is because the spacing of the Kiessig fringes is constant as a function of Q_z, but the width of each of the smearing kernels becomes broader as Q_z increases. Put simply, at low Q_z the kernels are just too narrow compared to the width of the features in the reflectivity curve.

3.1. Example 1 – thick trilayer film

Figs. 6(*a*) and 6(*b*) shows the simulated reflectivity from a trilayer film (Fig. 6*c*), with an overall thickness of 770 Å (Smith *et al.*, 2012). This simulation includes surface roughness effects. These figures show the unsmeared reflectivity (R_m), as well as the reflectivity convolved with the detailed and approximate smearing kernels ($R_{m,s}$). It is obvious from the difference plot in Fig. 6(*d*), and the reflectivity curves in Fig. 6(*a*), that the two different resolution kernels produce $R_{m,s}(Q_z)$ that are different for $0.07 < Q_z/\text{Å}^{-1} < 0.22$ – at one point reaching 20% difference. The oscillatory features in the two $R_{m,s}(Q_z)$ curves are out of phase in this region. The positive peaks in the difference plot correspond to minima in the unsmeared reflectivity, whilst the negative peaks correspond to the maxima in the unsmeared reflectivity. This is explored in more detail in Fig. 6(*b*), which shows both the reflectivities and both the kernels at a Q_z value of 0.1236 Å^{-1}. The out-of-phase nature arises because $p(Q_z)$ for the detailed kernel is less than $p(Q_z)$ for the approximate kernel within 1σ of the mean, with the situation reversing between 1σ and 2σ. Thus the approximate kernel has a heavier weighting towards the minima, whilst the detailed kernel has a greater contribution from the quickly rising reflectivities on either side of the minimum.

At $Q_z < 0.07$ Å^{-1} the difference between the two $R_{m,s}$ is small, because the width of the kernels is narrower than the

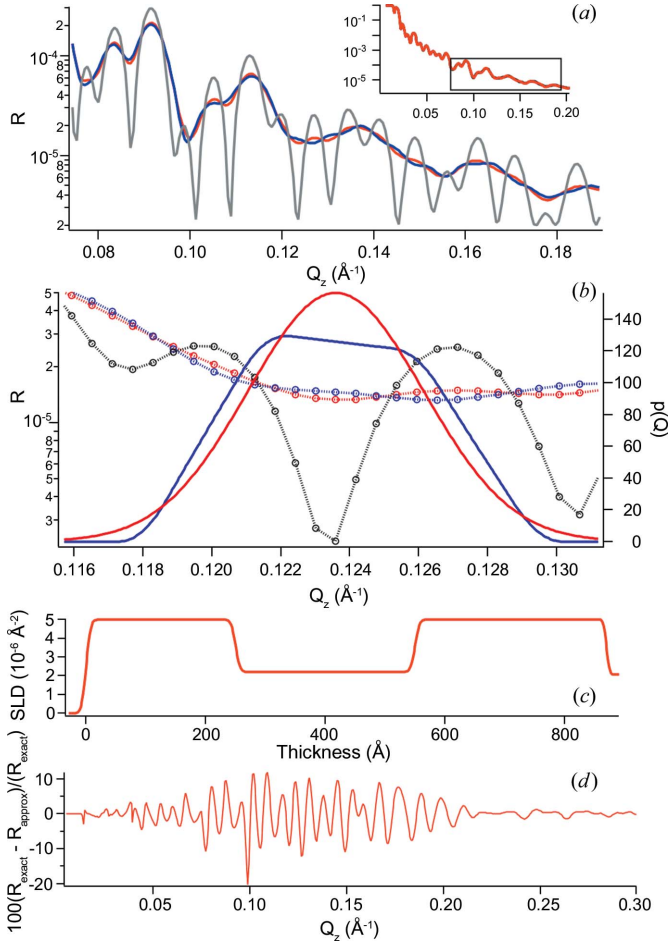

Figure 6
(*a*) Reflectometry from a model trilayer polymer film. The unsmeared reflectivity (grey) and the smeared reflectivity using the detailed (blue) and Gaussian (red) approximated resolution kernels are shown. The data were simulated at three non-overlapping angles of incidence, 0.5, 3.2 and 6°. The fractional angular and wavelength resolution components are the same as the instrument settings given in Fig. 5(*a*). (*b*) Zoomed plot around Q_z = 0.1236 Å^{-1}. The markers represent the reflectivity curves (left axis), and the solid lines represent the smearing kernels (right axis). (*c*) Scattering length density profile used to create the profiles in (*a*) and (*b*). (*d*) a difference plot between the detailed and Gaussian-approximated smeared reflectivities.

features in the unsmeared reflectivity. At $Q_z > 0.22$ Å^{-1} the difference between the two decreases as the background and interlayer roughness are more significant factors and the smearing kernels get very broad.

Even in the Q_z range where the reflectivity curves produced by the two kernels are observed to show the largest difference, it may be that this difference does not play a meaningful role in data analysis for a sample of this type. This is because counting statistics become increasingly worse at higher Q_z as the signal-to-noise ratio drops. Systematic errors, such as non-uniformity of the sample, or the coarseness of the chosen analysis model will reduce its importance. Nevertheless, there will be combinations of sample and measuring conditions where this effect will be significant. The most obvious situation is where wide wavelength resolution (much broader than the angular component), possibly with chopper phase opening, is used to maximize the flux onto a thick-film sample, either because it has a small area or because a kinetic study is desired. In such cases the breadth of the rectangular wavelength PDF dominates the overall resolution, resulting in a broad trapezoidal kernel that is skewed towards higher Q_z and quite unlike the Gaussian approximation.

3.2. Example 2 – critical edge of air–D_2O

The first derivative of a reflectivity curve is discontinuous at the critical edge. Rapid changes occur around the critical edge: below the critical edge the reflectivity is unity, with the reflectivity falling off quickly above the critical edge. Fig. 7 displays the critical edge region of an air–D_2O reflectivity profile, as measured on the Platypus instrument (James *et al.*, 2011). The PDF for the Gaussian and detailed kernels are also shown for $Q_z = 0.0174$ Å^{-1}. As discussed above, the Gaussian kernel is overweighted in the centre of the distribution, in contrast to the more detailed kernel, which is more heavily weighted towards the edges. Consequently, the Gaussian kernel underestimates the resolution smearing. In Fig. 7 this undersmearing is manifested in the Gaussian kernel fit, which

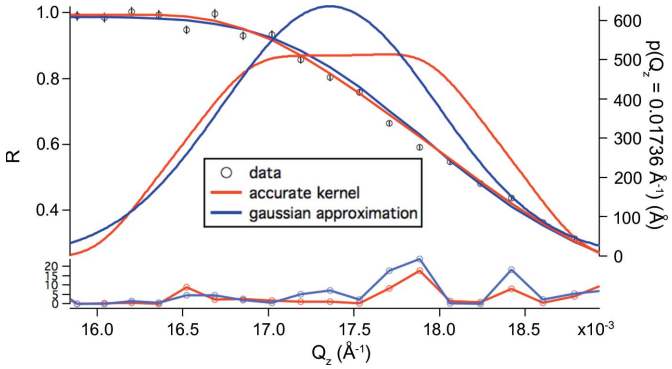

Figure 7
(Left-hand axis) Reflectivity from the critical edge region of an air–D_2O surface and the fits obtained using the detailed and Gaussian resolution kernels. (Right-hand axis) PDF for the detailed and Gaussian kernels for $Q_z = 0.0174$ Å^{-1}. (Bottom graph) squared normalized residuals. $d_1 = 2.368$ mm, $d_2 = 0.718$ mm, $L_{12} = 2800$ mm, $\theta_0 = 0.94^\circ$, $\tau_c/t = 0.0112$, rebinning at 2%.

significantly overpredicts the measured reflectivity in the region $0.0165 < Q_z/\text{Å}^{-1} < 0.018$. In comparison, the detailed kernel is able to describe the critical edge much more accurately; in the Q_z range 0.0155–0.0192 Å^{-1} the χ^2 value using the detailed kernel is 4.21, but the Gaussian kernel is 5.88. Moreover, the refined SLD values for the D_2O differ for the two kernels. Modelling using the Gaussian kernel predicts an SLD of $6.22\,(1) \times 10^{-6}$ Å^{-2}, whereas the detailed kernel predicts an SLD of $6.25\,(0) \times 10^{-6}$ Å^{-2} (the D_2O was not isotopically pure). If a fit is poor in the critical edge region this often has knock-on effects for the modelling of higher Q_z data. For example, in this situation the model would be forced to accommodate a lower SLD for the substrate, which would affect modelling of surface adsorbed layers, possibly changing their solvent content *etc*. This example shows the importance of using the detailed kernel for the correct description of the critical edge and its effect on modelled parameters.

3.3. Example 3 – multilayer film

Neutron reflectometers are often used to investigate multilayers that have a repeat structure similar to that of a regular crystal. Two examples are lipid diffraction and coatings used for neutron optics.

Multilayers with many repeats create Bragg peaks (Figs. 8 and 9). For a perfectly regular system (no mosaic spread, all repeats are identical) the Bragg peaks in the unsmeared reflectivity curve are extremely sharp, much narrower than $p(Q_z)$. Thus, when $p(Q_z)$ are convolved with the unsmeared data, the shape of the peaks should take on the shape of $p(Q_z)$ itself. This is akin to convolution with a delta function. Comparison of Fig. 8(*a*) with Fig. 5(*a*) shows that the smeared peak shapes are similar to the shape of the kernel used to do the convolution.

In practice it is difficult to deposit perfect films – lipid stacks have mosaic spread and sputtered metal films will show variations in thickness from layer to layer, correlated roughnesses and sample inhomogeneity over the measurement area. This will lead to an additional broadening of the measured peaks and significant off-specular scattering. Fig. 9 shows an NR measurement taken on the Platypus reflectometer (James *et al.*, 2011; Nelson, 2010) for an Ni/Ti multilayer. The SLD profile in Fig. 8(*b*) corresponds to the refined model from a least-squares analysis of the data presented in Fig. 9. An extra Gaussian broadening term (constant $\Delta Q_z/Q_z = 3.7\%$) was applied to the detailed and approximate kernels during the fitting process to account for variation in layer thickness over the stack and sample inhomogeneity. If this is not included then the peaks are wider than the width of either of the resolution kernels, for the reasons outlined above. A Gaussian broadening term was chosen in the absence of further information about sample inhomogeneity and on the basis that their cumulative effects would probably be Gaussian in nature as a result of the central limit theorem.

Fig. 9 clearly shows that the detailed kernel gives a much better fit than the approximate kernel. This is borne out in the χ^2 values from the fitting process – 9.6 for the detailed kernel,

but 20 for the Gaussian approximation – a huge improvement. The fits using either kernel give more or less the same model parameters within uncertainty. However, this is not unexpected as the location and area of the Bragg peaks are the dominant factors in determining layer thicknesses and scattering length densities (the number of repeats is known). Both kernels can more or less approximate these, even if the peak shapes can be improved. It is worth noting that the peak width is inversely related to the number of lattice repeat units *via* the Scherrer formula. In this example the number of repeat units is known. However, there are many systems (Hellsing & Rennie, 2011) where the number of repeat units is unknown and can be found *via* modelling. In those cases use of the Gaussian kernel will lead to an underestimation of the number of repeats as the fitting process has to compensate for the undersmearing of the data.

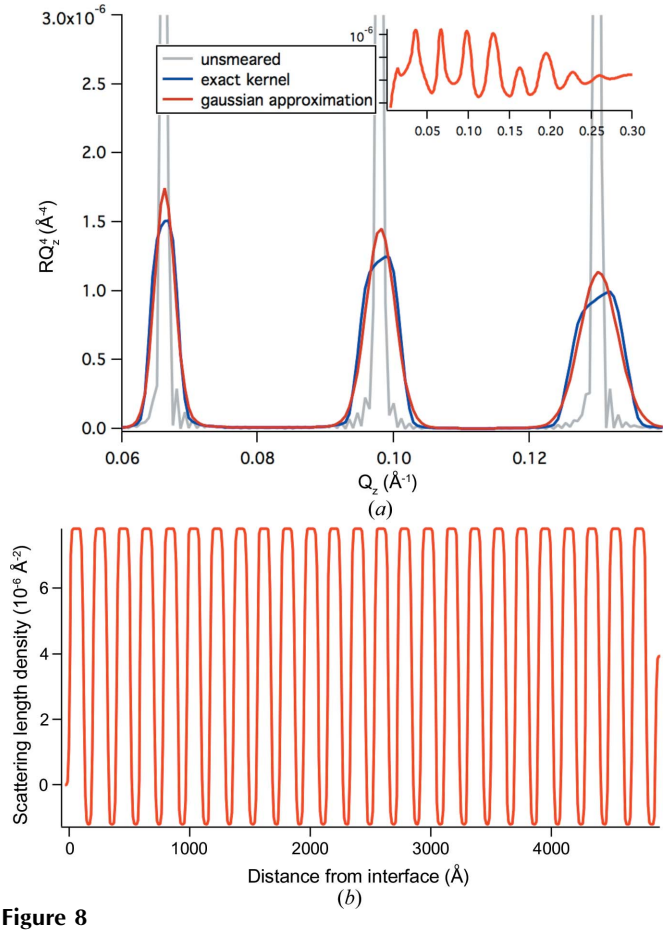

Figure 8
(*a*) Reflectivity from a simulated Ni/Ti multilayer with 25 bilayers, plotted as RQ_z^4 *versus* Q_z. The inset shows the convolved reflectivity over a wider Q_z range. The fractional wavelength and angular resolutions are the same as Fig. 5(*a*). (*b*) SLD profile of the interfacial region.

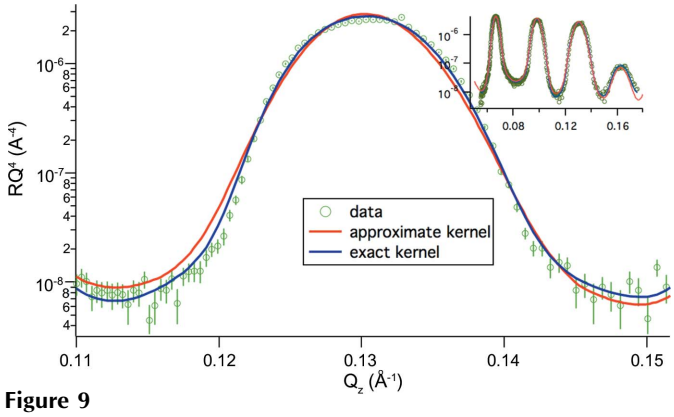

Figure 9
Measured reflectivity from an Ni/Ti multilayer (25 repeats) analysed with the detailed and Gaussian-approximated kernels. The analysis performed using the detailed kernel has a much lower χ^2 value (9.6) than the Gaussian approximation (20). The error bars on the data set are one standard deviation. The SLD model for this system is shown in Fig. 8(*b*).

4. Conclusions

I have outlined the form of the detailed resolution kernel for a reactor-based TOF neutron reflectometer and have compared it with its Gaussian approximation. These resolution kernels are typically convolved with theoretical reflectivity curves generated from model scattering length density profiles in a least-squares analysis. The choice of kernel used in the analysis process has the largest effect when the features of the reflectivity curve are similar in width to the resolution kernel: *i.e.* near the critical edge, or at high Q_z when thick films are being measured. The difference between the detailed and approximate kernels is maximized when there is a broad mismatch between the wavelength and angular components. These situations are typically encountered when the wavelength resolution is relaxed to facilitate measurement of small samples or experimental kinetics, but when the angular component cannot be relaxed in the same manner. In such cases the detailed resolution kernel becomes a broad trapezoid.

When the angular and wavelength components are similar in magnitude the detailed kernel becomes triangular in shape, and the choice of whether the detailed or approximate kernels are used is not as significant.

The original concept of investigating the detailed resolution kernel arose from ideas presented by Charles Dewhurst (Dewhurst, 2012). William Hamilton (Oak Ridge National Laboratory) is thanked for sharing some of the joys of the central limit theorem with me. John Barker and David Mildner (NIST) are thanked for critical review of the manuscript before submission.

References

Campbell, R. A., Wacklin, H. P., Sutton, I., Cubitt, R. & Fragneto, G. (2011). *Euro. Phys. J. Plus*, **126**, 107–129.
Cousin, F., Ott, F., Gibert, F. & Menelle, A. (2011). *Euro. Phys. J. Plus*, **126**, 109–119.
Dewhurst, C. D. (2012). *Proceedings of the 15th International Small-Angle Scattering Conference, Sydney, Australia, 18–23 November 2012*, edited by Duncan J. McGillivray, Jill Trewhella, Elliot P. Gilbert & Tracey L. Hanley. Lucas Heights: Australian Nuclear Science and Technology Organisation.
Dura, J. A., Pierce, D. J., Majkrzak, C. F., Maliszewsky, N. C., McGillivray, D. J., Lösche, M., O'Donovan, K. V., Mihailescu, M.,

Perez-Salas, U., Worcester, D. L. & White, S. H. (2006). *Rev. Sci. Instrum.* **77**, 074301.
Haan, V.-O. de, de Blois, J., van der Ende, P., Fredrikze, H., van der Graaf, A., Schipper, M. N., van Well, A. A. & van der Zanden, J. (1995). *Nucl. Instrum. Methods Phys. Res. Sect. A*, **362**, 434–453.
Hellsing, M. S. & Rennie, A. R. (2011). *Langmuir*, **27**, 4669–4678.
James, M., Nelson, A., Holt, S. A., Saerbeck, T., Hamilton, W. A. & Klose, F. (2011). *Nucl. Instrum. Methods Phys. Res. Sect. A*, **632**, 112–123.
Mueller-Buschbaum, P., Bauer, E., Maurer, E., Nelson, A. & Cubitt, R. (2007). *Phys. Status Solidi Rapid Res. Lett.* **1**, 68–70.
Nelson, A. (2006). *J. Appl. Cryst.* **39**, 273–276.
Nelson, A. (2010). *J. Phys. Conf. Ser.* **251**, 012094.
Smith, A. R. G., Lee, K. H., Nelson, A., James, M., Burn, P. L. & Gentle, I. R. (2012). *Adv. Mater.* **24**, 822–826.
Webster, J., Holt, S. & Dalgliesh, R. (2006). *Physica B*, **385–386**, 1164–1166.
Well, A. A. van & Fredrikze, H. (2005). *Physica B*, **357**, 204–207.